Advanced Energy Materials

ADVANCED ENERGY MATERIALS
www.advenergymat.de

RESEARCH ARTICLE OPEN ACCESS

Atomic-Scale Tracing of Lithium Trapped in Copper Current Collectors

Tong Li[1] | Carlo Franke[1] | Ziyuan Lyu[2,3] | Omair Ashfaq[2,3] | Mervyn Soans[2,3] | Mohsen Sotoudeh[2,3] | Thomas Diemant[2,3] | Jun Xia[1] | Aleksander Kostka[4] | Dominic Bresser[2,3,5]

[1]Faculty of Mechanical Engineering, Atomic-scale Characterisation, Ruhr-Universität Bochum, Bochum, Germany | [2]Helmholtz Institute Ulm (HIU), Ulm, Germany | [3]Karlsruhe Institute of Technology (KIT), Karlsruhe, Germany | [4]Zentrum Für Grenzflächendominierte Höchstleistungswerkstoffe (ZGH), Ruhr-Universität Bochum, Bochum, Germany | [5]Ulm University (UUlm), Ulm, Germany

Correspondence: Tong Li (tong.li@rub.de) | Dominic Bresser (dominic.bresser@kit.edu)

Received: 17 February 2026 | **Revised:** 23 June 2026 | **Accepted:** 29 June 2026

Keywords: atom probe tomography | battery | copper | current collector | lithium

ABSTRACT

Zero-excess lithium-metal batteries (LMBs) are expected to provide the maximum energy density in combination with classic lithium-containing cathode materials. However, the lithium plating process on a blank current collector suffers from huge irreversibility, thus, causing rapid capacity fading. Herein, we employ atom probe tomography to track the occurring lithium losses. The results unambiguously reveal that lithium is trapped at grain boundaries and junctions in the copper foil after the first cycle—not only on the copper foil as commonly assumed – with a local concentration up to ~28 at.% at the boundary junctions. After continuous plating and stripping, the copper foil subsurface regions (~100 nm) become nanocrystalline, creating additional defects. These defects facilitate further trapping of lithium, along with oxygen and carbon, in the subsurface region of the copper foil. Such compositional and structural changes in the copper foil surface may contribute to the degradation of the current collector during cycling, which has so far been largely overlooked in discussions of LMB performance decay.

1 | Introduction

Lithium-metal batteries (LMBs) are considered the next big step forward toward the development of higher energy density batteries, owing to the very low redox potential of −3.04 V vs. the standard hydrogen electrode and its exceptionally high theoretical specific capacity of 3860 mAh g^{-1} [1–3]. For this reason, lithium-metal negative electrodes have long been regarded as the "holy grail" for next-generation batteries [4, 5]. However, the high reactivity of lithium metal with essentially any of the commonly used electrolytes and the remaining risk of dendritic lithium deposition still hamper its widespread commercial application [1, 6, 7]. In this context, "zero-excess" (also called "anode-free") LMBs, in which lithium from the positive electrode is essentially simply plated on a "blank" current collector upon charge, have recently attracted rapidly increasing interest, as these promise even higher energy densities and substantial cost reduction, and there is no need to handle and process highly reactive lithium-metal foil [8–12].

The most studied current collector in "zero-excess" LMBs is the copper foil. The choice of copper originates from the commonly accepted view that copper is inert in contact with metallic lithium at such low potentials [13–16]. However, only very few studies have investigated this in more detail, finding that there is, in fact, an irreversible "trapping" of lithium in copper using characterization techniques such as inductively coupled plasma – atomic emission spectroscopy [17], neutron depth profiling (NDP) [18], and time-of-flight secondary mass spectrometry [19]. The amount of lithium being irreversibly trapped inside the copper

foil, however, varies quite significantly between these studies, ranging from 4 to 10 μg cm^{-2} [17, 18]; with the former value being obtained after electrochemical lithium plating on copper.

Essentially, lithium trapping sites remain rather elusive. It has been proposed by molecular dynamics simulations that lithium might preferably enter the grain boundaries in polycrystalline copper foils, while an ex situ x-ray diffraction analysis did not reveal any detectable changes in the crystal structure of the copper foil [20]. Rupp et al. [19], though, reported that there is also lithium diffusion into the bulk copper foil when comparing the impact of (i) bringing lithium in direct contact with copper, (ii) polarizing the copper foil in contact with a lithium salt-containing electrolyte, and (iii) high-energy lithium implantation – for polycrystalline and single-crystalline copper foils. Nevertheless, a clear experimental proof of the position and distribution of lithium within copper metal foils, as well as precise quantification that excludes any contribution from lithium-containing electrolyte decomposition products, is missing in the literature, since the techniques used so far lack sufficient spatial resolution and compositional analytical capabilities. Therefore, new characterization tools that can provide nanoscopic elemental and compositional details in local regions, such as grain boundaries, are needed to trace lithium trapped in the copper foil.

Atom probe tomography (APT) can provide three-dimensional (3D) spatial distribution and composition data for both light and heavy elements in solid materials, with parts-per-million chemical sensitivity at a sub-nanometer spatial resolution [21]. Herein, we employ APT to trace where lithium is trapped and its concentration at local regions after one and three plating/stripping cycles in a Li||Cu cell using an ionic liquid-based electrolyte. The aim of this study is to elucidate the lithium trapping sites in the copper foils after the first few cycles. In addition, scanning transmission electron microscopy (STEM) and transmission Kikuchi diffraction (TKD) were combined with APT to investigate the microstructural changes of the copper foil. To corroborate these atomistic observations, depth-resolved x-ray photoelectron spectroscopy (XPS) was also employed to complement the determination of the chemical state of the trapped species and the evolution of the solid electrolyte interphase (SEI). We found that lithium is initially trapped at the grain boundaries and boundary junctions after one plating/stripping cycle. Surprisingly, after only two more plating/stripping cycles, the copper foil surface becomes nanocrystalline and oxidized, and the newly formed defects and oxygen further trap lithium in the sub-surface region. As the number of cycles increases (to eight), more lithium is accumulated in the grain interior and at the grain boundaries of the copper foil.

2 | Results and Discussion

For investigating the potential lithium trapping in a copper current collector, we assembled Li||Cu pouch cells (Illustration of stripping plating process shown in Figure 1a) employing a proven electrolyte composed of a mixture of 1-butyl-1-methyl pyrrolidinium bis(fluorosulfonyl)imide ($PYR_{14}FSI$) and lithium bis(trifluoromethanesulfonyl)imide salt (LiTFSI) with a ratio of 8:2 ($PYR_{14}FSI$:LiTFSI) and 5 wt.% of fluoroethylene carbonate (FEC) [22]. These cells were subjected to one, three, and eight lithium plating and stripping cycles to assess lithium trapping in the copper current collector with increasing cycle number (cf. the schematic illustration in Figure 1b). The plating/stripping profiles for cells with one, three, and eight lithium plating and stripping cycles are displayed in Figure 1c,d,e. The plating step can be divided into three characteristic regimes, as indicated in the inset of Figure 1c. In *Regime 1* (in red), the cell voltage drops steeply as soon as a current is applied. The (very minor) non-linearity can be assigned to electrolyte decomposition, resulting (in part) in the formation of a "solid electrolyte interphase" (SEI) – more precisely, maybe in this context, in a (partially) passivating surface layer composed of electrolyte decomposition products. Subsequently, in *Regime 2* (in blue), lithium metal nucleates on the copper foil, forming lithium metal deposits, accompanied by a nucleation overpotential. In *Regime 3* (in black), the cell voltage shows a plateau, which is related to the lithium plating on the copper foil [22–24]. The plating/stripping efficiency, i.e., the Coulombic efficiency, is less than 70% for the first plating/stripping cycle and increases to around 85% for the third cycle and to around 90% from the fifth cycle onward. This indicates a large irreversibility in the first cycle and a still substantial irreversibility in subsequent cycles, which is commonly attributed to the aforementioned electrolyte decomposition and the formation of "dead lithium", i.e., lithium that is, for some reason, no longer accessible upon further plating and stripping [25, 26].

After one, three, and eight plating/stripping cycles, the Li||Cu pouch cells were disassembled in an argon-filled glovebox, along with a non-cycled Li||Cu pouch cell serving as reference. The non-cycled and cycled copper foils were rinsed five times with 1,2-dimethoxyethane to remove residual electrolyte. Subsequently, the copper foils were transferred via a high-vacuum transfer suitcase to a scanning electron microscope (SEM) equipped with a focused ion beam (FIB) for TEM and APT specimen preparation. Transferring the as-cleaned copper foils under high vacuum conditions between the glovebox, FIB/SEM and APT is essential for ensuring a precise characterization of their 'native' state by APT and scanning transmission electron microscopy (STEM in FIB/SEM), since metallic lithium and electrolyte decomposition products can be maintained in their "as-formed" state on the surface of the copper current collector foils. They are highly reactive toward the ambient atmosphere. Also, blank copper is readily oxidized in air when the native passivation layer is removed during cycling (e.g., as a result of the reaction with lithium upon plating). The SEM micrographs in Figure 2a–c, i.e., the top-down views of the copper foils, reveal that electrolyte decomposition product layers remain on the surface after rinsing (cf. the pristine copper foil surface depicted in Figure S1). The electrolyte decomposition product layer appears difficult to be removed from the one-cycle copper foil surface, even after rigorous rinsing, since the majority of the surface is covered by this layer (Figure 2a), concealing the grooves that were observed for the pristine copper foil (Figure S1) and the three- and eight-cycle copper foil surfaces (Figure 2b,c). The electrolyte decomposition product has a thickness of ~220 nm (see Figure 2d, recorded from a TEM lamella showing the cross-section of the one-cycle copper foil prepared from the red rectangular region in Figure 2a). Ex situ XPS depth profiling analysis shows that the SEI layer is generally composed of an organic, i.e., C/O-rich outer layer and an inorganic-rich, e.g., Li_2O and LiF, inner layer (see

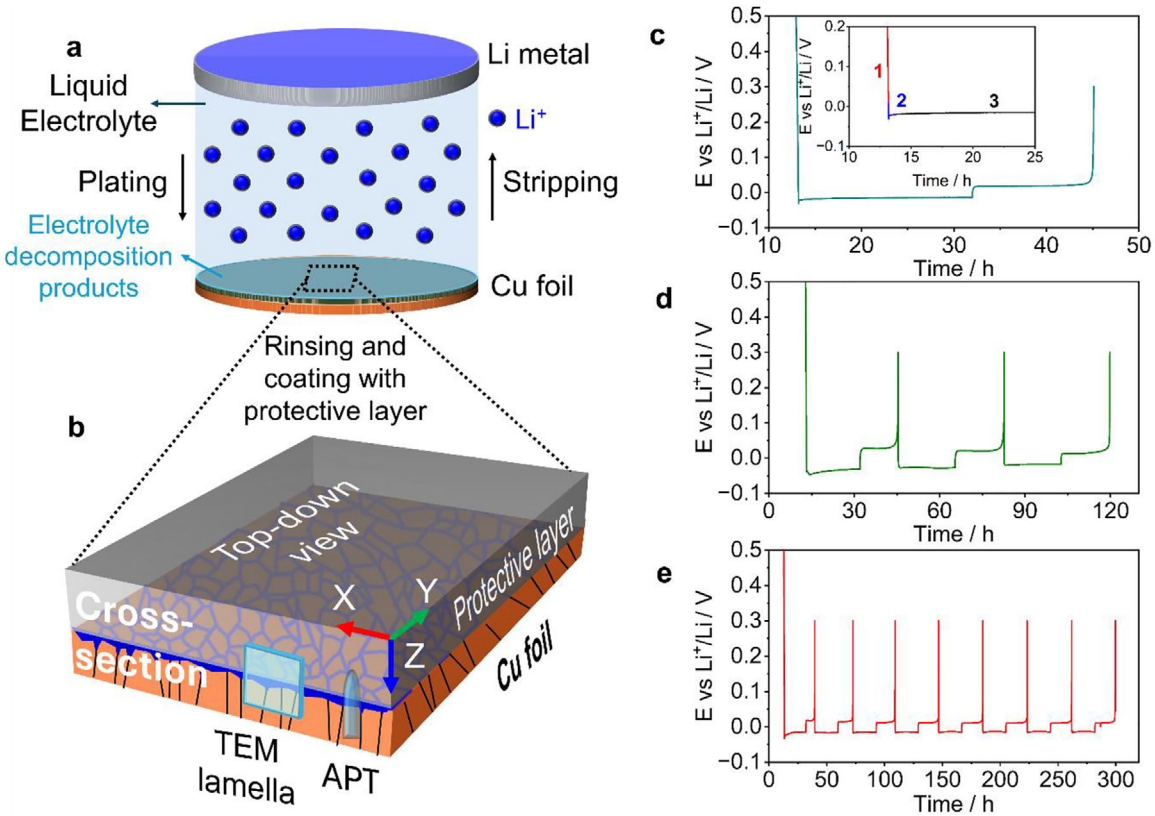

FIGURE 1 | Cell setup and galvanostatic lithium plating and stripping. (a) Illustration of lithium plating and stripping process on the copper current collector. (b) Schematic diagram showing the TEM lamella and APT specimens prepared in the center of the copper current collector after cleaning in DME and coating of a protective layer. (c,d) Voltage profiles recorded for the Li|Cu cells subjected to (c) one, (d) three, and (e) eight plating/stripping cycles; the inset in (c) shows the three characteristic regimes of the initial plating step.

Figure S2 along with the detailed discussion of the findings in the Supporting Information), in good agreement with previous studies [6]. The formation of such electrolyte decomposition products contributes to the initial capacity loss and the rather low coulombic efficiency.

After three plating/stripping cycles, some electrolyte decomposition products remain as isolated particles, exhibiting dark contrast in Figure 2e and brighter contrast in Figure 2b on the copper foil surface. The ex situ XPS depth profiling analysis reveals a similar organic-to-inorganic stratification (Figure S3). With an increased sputtering depth, the SEI again evolves toward an inorganic-rich composition with increasing contributions from LiF and Li_2O. Notably, metallic lithium (Li 1s at ~52.5 eV) [27] is detected throughout the depth profile, with increasing intensity toward the buried interface. A concurrently emerging Cu $2p_{3/2}$ signal confirms that sputtering is progressively approaching the Cu substrate (see Table S1 and Note S1), although the SEI layer was not fully penetrated. This suggests that lithium may be trapped in the copper current collector or at rough interfaces between the electrolyte decomposition products and the copper foil surface.

Remarkably, as a first observation, the inset of the STEM image of the three-cycle sample, Figure 2e, reveals that the copper foil surface appears ruptured compared to that after one cycle (inset in Figure 2d). To further investigate the microstructural changes in the copper foil, TKD was performed on the same TEM lamellae. TKD provides electron backscatter diffraction data with enhanced spatial resolution, revealing grain orientations [27]. The orientation contrast map in Figure 2h shows that the top surface regions of the three-cycle copper foil contain more nanocrystals than those after one cycle (Figure 2g). Taking a closer look at the copper foil surfaces using STEM, we clearly see, from Figure 2k, that the top ~100 nm subsurface region becomes nanocrystalline. In comparison, the one-cycle copper foil surface is relatively smooth and flat, and no nanocrystals were observed (Figure 2j). As the cycle number increases to eight, the top 100 nm of the copper foil surface remains ruptured (inset in Figure 2f). The copper foil surface is heavily deformed, as revealed by the TKD mapping in Figure 2i. Upon closer inspection of the copper foil surface, more defects are present in the top 50 nm, below which stacks of ~100 nm nanocrystals are formed (Figure 2l). Our TKD and STEM images (Figure 2g–l) unambiguously show that the grain size on the copper foil surfaces decreases from micrometer-sized grains to nanocrystals as the number of cycles increases. Notably, the copper foil was subjected to eight plating/stripping cycles – not hundreds or even thousands, as needed for rechargeable batteries. This suggests that the copper foil surface undergoes microstructural changes even after a short cycling duration, likely due to stress- or strain-induced severe plastic deformation, as is often observed in copper when used as a structural material [28]. A recent theoretical study [29] proposed that a stress gradient in the copper current collector can be generated by stresses associated with lithium plating and stripping processes, whereby lithium diffuses into

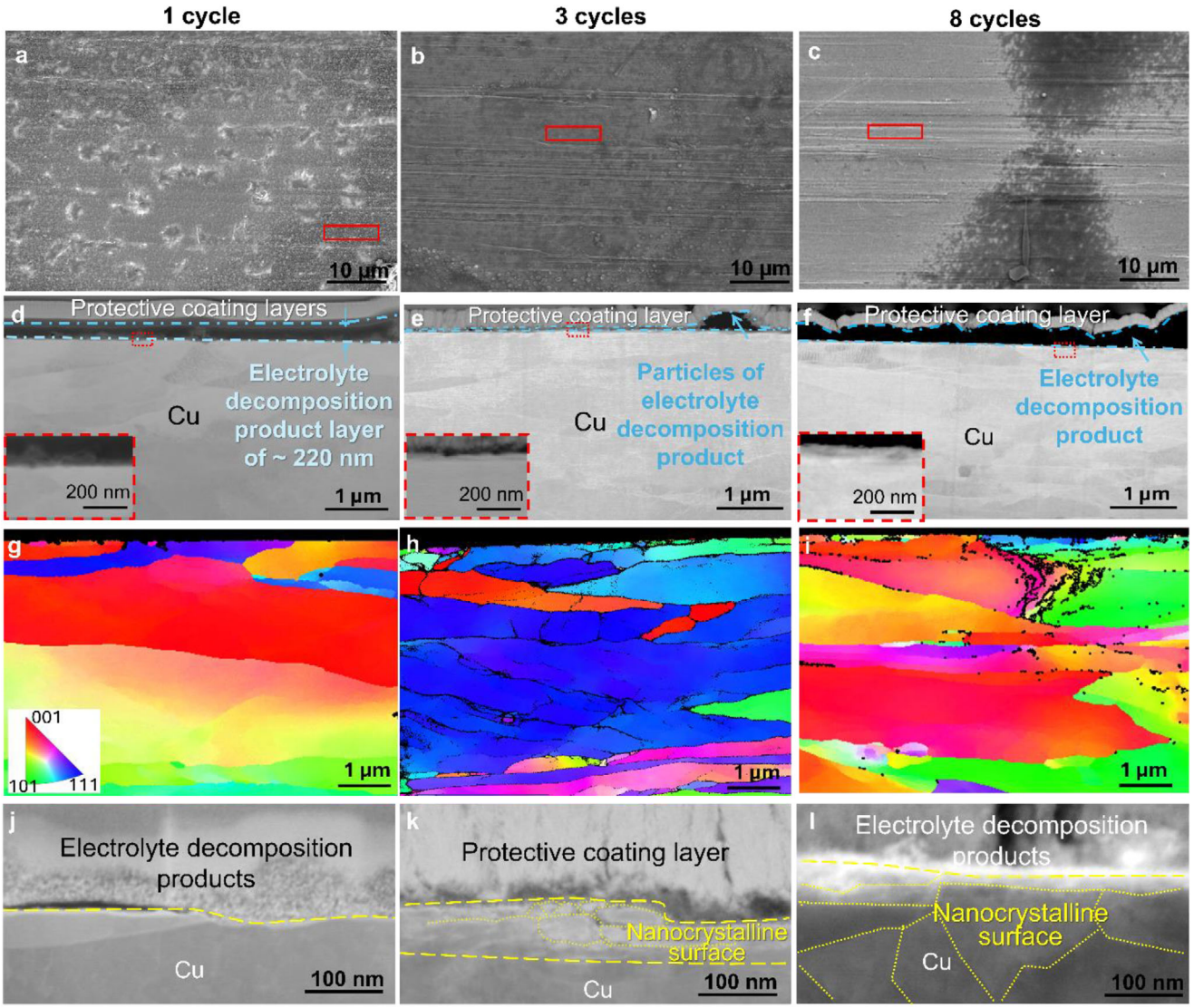

FIGURE 2 | Top-down and cross-section view of the copper current collector after one and three plating/stripping cycles. (a–c) SEM micrographs showing the top-down view on the cleaned copper foil after (a) one, (b) three, and (c) eight plating/stripping cycles. (d–f) Low-resolution STEM/high-angle annular dark-field (HAADF) images showing the cross-section of the copper foil after (d) one, (e) three and (f) eight cycles, with insets showing the magnified regions marked by the red-boxes in (d–f). The TEM lamellae prepared from the red-box regions in (a–c) respectively. (g–i) Orientation contrast maps recorded by transmission Kikuchi diffraction of the cross-section of the copper foil after (g) one, (h) three and (i) eight plating/stripping cycles (from the same TEM lamellae in (d), (e), (f) respectively). (j–l) Magnified view of the STEM/dark-field images of the cross-section of the copper current collector after one, three and eight plating/stripping cycles.

the copper current collector. Our study demonstrates that this stress gradient also induces microstructural changes in the top ~100 nm subsurface region of the copper current collector, where additional defects, such as vacancies, dislocations, and interfaces, may, in turn, enhance lithium diffusion in the copper current collector with increasing cycles.

To investigate the lithium trapping in the copper current collector, APT was performed on the copper foils after one and three plating/stripping cycles (three to five datasets were obtained for each experiment). APT is a mass-spectrometry technique that allows for the reconstruction of 3D maps of atomic structures with near-atomic resolution from needle-shaped specimens [21]. The reconstructed APT data take the form of 3D point clouds, where each colored dot represents an individual ion detected and elementally identified. We can see in Figure 3a, a specimen prepared from the top surface of the copper foil after one cycle, that lithium (in blue) is unevenly distributed in the copper foil (in orange) (as also observed in two additional APT datasets in Figure S4a,b). When rotating the 3D-reconstructed data, we can clearly see that the lithium distribution resembles two planes, indicative of grain boudaries, as shown in Video S1 at around 6 and 11 s. Essentially, the activation energy for lithium diffusion through the copper lattice is ~0.68 eV [18]. In contrast, the activation energy for lithium diffusion along copper grain boundaries is ~0.36 eV, indicating that diffusion along the copper grain boundaries is energetically favorable. Our atomic-scale result unambiguously confirms that lithium is initially trapped at grain boundaries in the copper foil after the first plating and stripping cycle.

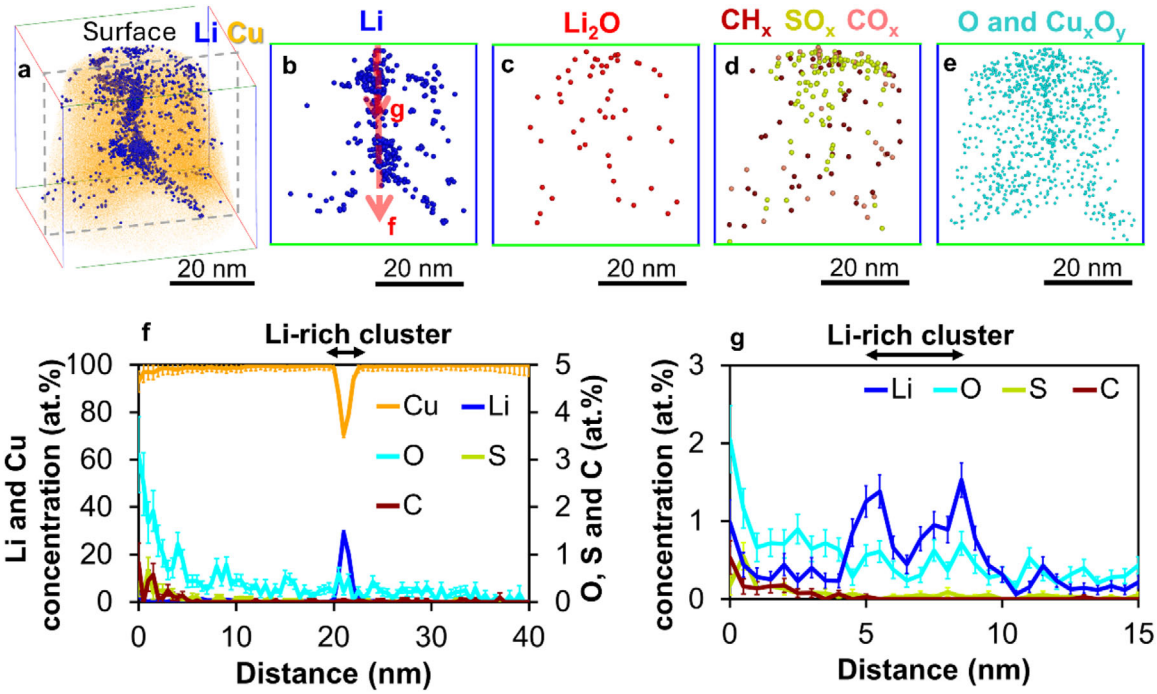

FIGURE 3 | Detection of lithium in the copper current collector after one plating/stripping cycle. (a) 3D-APT reconstructed data revealing the trapping of lithium in the grain boundaries present in the copper foil. (b-e) Atom maps from the grey dashed region in (a), displaying the distribution of (b) Li, (c) Li_2O, (d) $CH_x/SO_x/CO_x$, and (e) O-containing molecular ions. (f) 1D Concentration profiles plotted along the grain boundary and boundary junction shown in (b) marked f. (g) 1D Concentration profiles from the top 15 nm region of (f) marked g in (b).

Additionally, lithium trapping along the grain boundaries is rather non-uniform, as revealed by the cross-sectional atom maps presented in Figure 3b (a 5 nm slice in the grey-dashed region in Figure 3a). This might be due to lithium diffusing into grain boundaries driven by the stress gradient during plating (in addition to the force induced by the electric field) [29]. Upon stripping, it appears that some lithium is unable to exit from the grain boundaries and is pinned at, e.g., boundary junctions, as revealed by the ~3 nm lithium-rich cluster at the grain boundary junction observed in Figure 3b. The lithium concentration is up to 27.8 ± 0.5 at.% in the lithium-rich cluster at the boundary junction, as shown by the 1D concentration profile in Figure 3f (plotted by placing an analysis cylinder along the red arrow f in Figure 3b). Notably, lithium was found to be not easily alloyed with copper [30], although the solubility of lithium in copper is about 12–16 at.% at room temperature according to the copper-lithium phase diagram [31, 32]. The considerable amounts of lithium at the boundary junction are likely arising from substantial amounts of vacancies and dislocations at the grain boundaries, especially at junctions, which alter the thermodynamic equilibrium as predicted by the phase diagram [33, 34]. In the top region of the grain boundaries, a ~4 nm lithium-rich cluster was also observed, but with a concentration of 1–1.5 at.%, as revealed by the 1D concentration profile in Figure 3g (plotted along the arrow g in Figure 3b). In addition to lithium trapped at the grain boundaries and junctions, some lithium is also trapped in the grain interior with a concentration of 0.04 ± 0.01 at.%, as summarized in Table 1 and revealed in Figure 3b. Notably, the non-cycled copper foil also contains a rather dilute amount of Li, i.e., 0.003 ± 0.001 at.% as impurities (see Table S2, summarized from two APT datasets of pristine copper foils), significantly lower, though, than the Li concentration in the grain interior after one and three cycles. This means that lithium diffuses not only along grain boundaries but also into the grains. Grain boundary junctions containing more vacancies and dislocations can trap more lithium, making inward or outward diffusion during plating or stripping more difficult, in turn leading to the formation of 3–4 nm-sized lithium-rich clusters at the grain boundaries and boundary junctions.

Besides lithium, oxygen-, carbon-, and sulfur-containing complex molecular ions were also detected on the surface and inside the copper foil, such as Li_2O (Figure 3c), C, CH_3 and CH_4 (shown as CH_x in Figure 3d), CO and CO_2 (CO_x shown in Figure 3d), S and SO (SO_x, Figure 3d), O, CuO, CuOH, CuO_2 species (shown as O and Cu_xO_y in Figure 3e). These complex molecular ions are fragments from the electrolyte decomposition products during field evaporation of APT measurements (see the mass spectra in Figure S5a). Note that the thick electrolyte decomposition product layer was not detected by APT, likely due to fractures induced by field evaporation. Instead, the APT data in Figure 3 shows elemental distributions from the copper surface to the bulk (Figure 3a–e). CH_x, SO_x, and CO_x molecular ions are mainly located on the surface. In contrast, O and Cu_xO_y molecular ions are distributed across the top 40 nm surface regions, with slightly higher atomic oxygen concentration at the grain boundary (0.28 ± 0.05 at.% in Table 1) than in the grain interior (0.17 ± 0.01 in Table 1). Given the low oxygen content, oxygen is thought to diffuse into interstitial sites and vacancies in the copper lattice rather than forming copper oxides. A previous in situ TEM study [35] observed that impurity oxygen atoms can be embedded in the lithium crystals inside the graphene sheets during lithiation, and these oxygen atoms play a key role in trapping lithium in the graphene upon delithiation. Hence, we speculate that the oxygen trapped in the copper foil might also contribute to the irreversible

TABLE 1 | Composition in different regions of the copper foil after one, three, and eight lithium plating/stripping cycles.

Element	1 cycle			3 cycles			8 cycles		
	Grain interior	Li-rich cluster at boundary junctions	Surface regions	Grain interior	Surface Li-rich regions	Bottom Li-rich regions	Grain interior	Surface Li-rich regions	Li segregation at grain boundary
Li	0.04 ± 0.01	27.8 ± 0.5	0.33 ± 0.02	0.08 ± 0.01	42.9 ± 0.5	3.2 ± 0.1	0.34 ± 0.01	70.8 ± 0.6	45.5 ± 1.3
Cu	99.8 ± 0.1	71.9 ± 0.8	98.7 ± 0.4	98.7 ± 0.1	48.4 ± 0.5	95.2 ± 0.4	98.2 ± 0.2	18.8 ± 0.3	54.3 ± 1.4
O	0.17 ± 0.01	0.28 ± 0.05	0.72 ± 0.03	1.1 ± 0.1	4.6 ± 0.2	1.1 ± 0.1	1.30 ± 0.02	4.7 ± 0.1	0.22 ± 0.09
C	0.01 ± 0.01	0.05 ± 0.02	0.10 ± 0.01	0.02 ± 0.01	0.35 ± 0.04	0.49 ± 0.03	0.04 ± 0.00	0.47 ± 0.04	—
N	—	—	—	0.02 ± 0.01	0.12 ± 0.03	0.02 ± 0.01	0.02 ± 0.00	0.21 ± 0.03	—
S	0.01 ± 0.01	—	0.14 ± 0.01	0.07 ± 0.01	0.68 ± 0.06	0.06 ± 0.01	0.09 ± 0.01	0.13 ± 0.02	0.04 ± 0.04
F	—	—	—	0.02 ± 0.01	3.0 ± 0.1	—	0.01 ± 0.01	4.83 ± 0.14	—

lithium trapping, as also previously suggested by an NDP study [18].

After three plating/stripping cycles, lithium-rich regions are present not only on the surfaces but also ~70 nm below the copper surface (Figure 4a,b). The rotational 3D-APT reconstruction, shown in Video S2, reveals that lithium is distributed as linear-, planar-, and particle-like features in the subsurface region; two additional APT datasets in Figure S4c,d also reveal similar lithium-rich features below the copper foil surfaces. This result aligns well with our observation in Figure 2k that the top 100 nm of the copper foil surface becomes defect-rich after three cycles. An increasing number of defects, i.e., vacancies, dislocations, and nanocrystal interfaces, are generated in the top 100 nm of the three-cycle copper foil, which likely trap lithium easily, leading to the formation of lithium-rich features in the subsurface regions. Specifically, the sub-surface lithium-rich linear or planar features have a lithium concentration of 3.2 ± 0.1 at.%, as revealed by the 1D concentration profile shown in Figure 4f and Table 1. This is lower than the surface lithium concentration (~43 at.%), where lithium-containing electrolyte decomposition products are present. In addition, more lithium (0.08 ± 0.01 at.%) is found in the grain interior after three cycles compared to 0.04 ± 0.01 at.% of lithium after one cycle (cf. Table 1). This suggests that lithium can continuously diffuse into the copper lattice as the cycle number increases.

Also, in addition to Li_2O, CH_x, SO_x, CO_x, and O/Cu_xO molecular ions, Li_2F and N-containing complex molecular ions are significantly enriched and clearly resolvable after three cycles in Figure 4c–e (see the mass spectra in Figure S5b,c). This suggests that inner inorganic-rich electrolyte decomposition products were detected by APT, as indicated by the XPS results in Figure S3. Our APT data shows that Li_2O and Li_2F (Figure 4c), as well as CH_x, SO_x, CO_x, and N (Figure 4d), are distributed non-uniformly in the form of separate nanodomains. Li_2O, Li_2F, and CO_x are mainly detected in the top 10 nm surface regions (Figure 4c,d), whereas N and SO_x are distributed in the top ~20 nm region. In comparison, O/Cu_xO_y molecular ions are present across the top 100 nm region (Figure 4e). The atomic O concentration locally reaches ~16 at.% in the top 30 nm of the surface, as shown in Figure 4g, which is significantly higher than that after one cycle (Figure 3f). This suggests that the copper foil surface is likely to be locally oxidized in the Cu foil sub-surface regions.

More interestingly, Li_2O (red dots in Figure 4c) and CH_x (brown dots in Figure 4d) molecular ions are also observed in the sub-surface ~70 nm region (Figure 4c–e and Video S3). We may speculate that carbon- and oxygen-containing electrolyte decomposition products might be unstable, further decomposing into carbon and oxygen and diffusing into the subsurface. In comparison, F-, S-, and N- containing electrolytes and decomposition products are relatively stable, leading to their absence in the sub-surface regions. The oxygen and carbon concentrations are ~2 and ~1 at.% in the sub-surface areas (Table 1). Intriguingly, oxygen and carbon are co-located with lithium-rich features in the subsurface regions. This provokes us to speculate if oxygen and carbon, especially oxygen, further induce lithium trapping in copper. To further interrogate this, atom maps of Li, Li_2O, C_xH_y, and O/Cu_xO_y were plotted from two regions to compare their distribution in the lateral plane (Figure S6). We can see that Li_2O is distributed within the lithium-concentrated regions (delineated by magenta-dotted lines), which are covered by C_xH_y species as a shell layer (Figure S6b–d,g–i). In addition, the overall O/Cu_xO_y distribution covers a wider area than the lithium distribution (black-dotted lines, Figure S6e,f,j,k). Thus, an onion-like structure, Li_2O in the core, followed by lithium, carbon, and O/Cu_xO_y in the shell, is present in the sub-surface of three-cycle copper foil. Such features suggest that the diffusion of lithium, oxygen, and carbon in copper likely occurs via different processes at successive cycles: lithium diffuses into copper defect sites upon plating, whereas oxygen and carbon, especially oxygen,

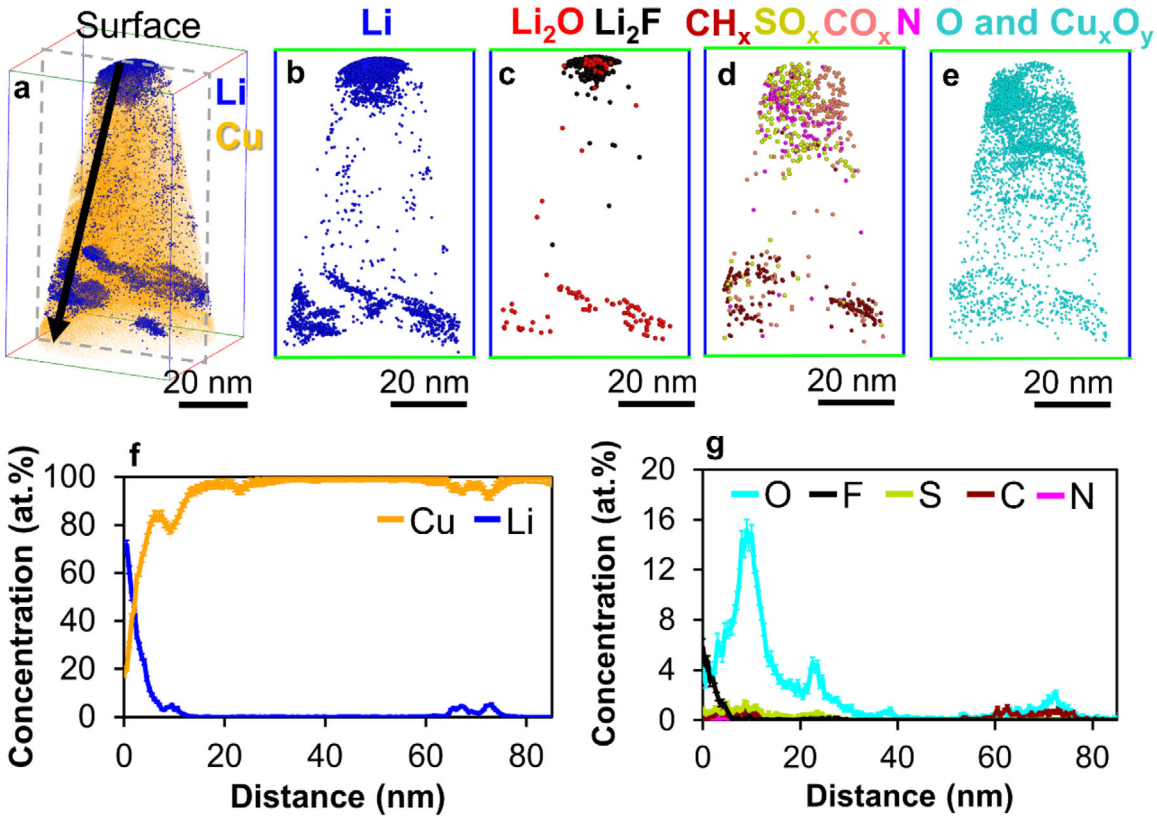

FIGURE 4 | Detection of lithium in the copper current collector after three plating/stripping cycles. (a) 3D-APT reconstructed data showing the presence of Li on the surface and ~60 nm region below the surface. (b-e) Atom maps from the grey dashed region in (a) revealing the distribution of (b) Li, (c) Li_2O/Li_2F, (d) $CH_x/SO_x/CO_x/N$ and (e) O-containing molecular ions. (f) 1D Concentration profile plotted along the arrow in (a) showing only the lithium and copper content. (g) The same 1D concentration profiles as in (f), but showing the atomic O, F, S, C, and N content.

might diffuse into copper during stripping. In fact, copper is easily oxidized at room temperature [36]. Its affinity for oxygen and ability to lose electrons are enhanced at a positive potential during stripping, when oxygen might be preferentially trapped and stabilized at defect sites, such as dislocations and nanocrystal interfaces generated in the copper sub-surface during cycling. Such oxygen segregation at defect sites may trap lithium during subsequent plating, thereby further driving the diffusion of oxygen and carbon upon subsequent stripping, in which onion-like features accumulate on the subsurfaces of the copper foil.

To complement our observations from a thermodynamic perspective, density functional theory (DFT) simulations were performed to evaluate the energetics of lithium incorporation into copper and its interactions with oxygen and carbon (Figures S7 and S8, Table S3, and Note S2). The DFT results show that lithium incorporation at copper vacancy sites is highly favorable (−1.64 eV) compared to that in a perfect copper lattice (+2.26 eV; Table S3). Moreover, lithium exhibits a rather strong interaction with oxygen, forming a Li—O bond with a length of ~1.81 Å (Table S3, Figures S7 and S8a). Remarkably, oxygen is largely separated from other oxygen atoms by a distance of ~2.92 Å, suggesting that oxygen is likely stabilized at defects such as vacancies or dislocations. In comparison, lithium interacts less strongly with carbon, but the Li—C bond is still energetically favorable (−3.21 eV), explaining why carbon segregates to the shell of lithium-rich regions in Figure S6d,i. In brief, the DFT simulation indicates that defects and oxygen can act as strong trapping sites for lithium upon successive plating and stripping cycles, corroborating the APT data and the conclusion that oxygen, along with defects, can attract and pin lithium during cycling.

Upon increasing the cycle number to eight, stacks of nanograins of ~100 nm form in the subsurface regions of the copper foil (Figure 2l). The APT data, shown in Figure 5, capture grain boundaries in the subsurface regions, as clearly depicted by the lithium-rich planar features (Figure 5a,b and Video S4); an additional APT dataset also shows grain boundaries (Figure S4f). The lithium concentration at the grain boundaries is up to 45.5 ± 1.3 at.% as revealed by the 1D concentration profile in Figure 5f, plotted perpendicular to the grain boundary. The composition at the grain boundary, on the surface, and within the copper grain interior is summarized in Table 1. By comparing the lithium-rich clusters formed at the grain boundary junction after one cycle, we can conclude that the lithium concentration at the grain boundary after eight cycles increases significantly (Table 1). Notably, the grain boundary is composed of linear dislocation features that serve as trapping sites for lithium (see the linear features after 8 s in Video S4). The dislocations closer to the copper foil surface pin more lithium (~45 at.%) compared to those far away from the surface (~20 at.%), as revealed by the 1D concentration profile plotted along the grain boundary from top to bottom (Figure S9). In addition to trapping at the grain boundaries, lithium is also present on the copper foil surface, most likely due to the presence of electrolyte decomposition products, since Li_2O, LiF, CH_x, SO_x, CO_x, and N are also collocated with lithium in the surface region

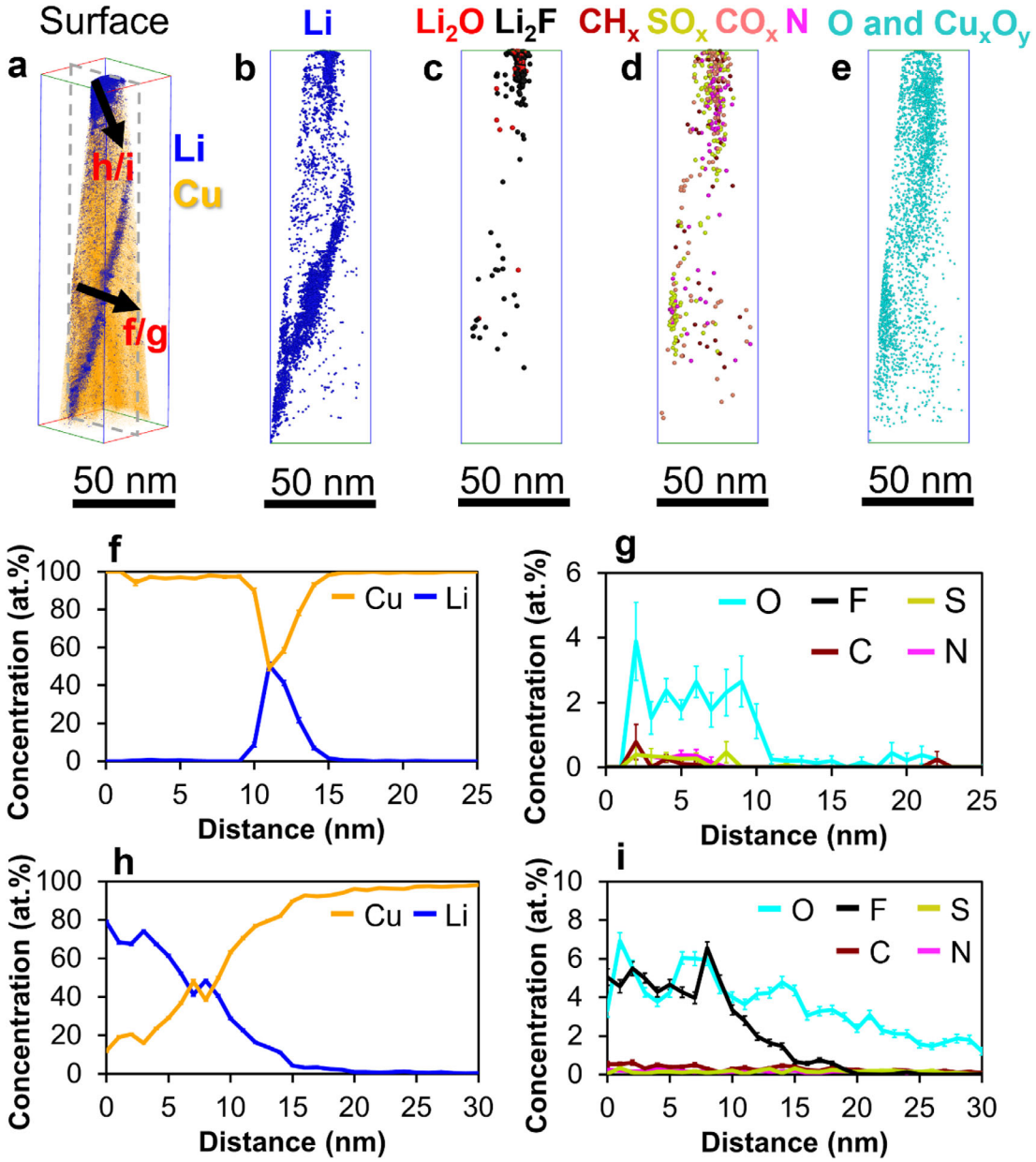

FIGURE 5 | Detection of lithium in the copper current collector after eight plating/stripping cycles. (a) 3D-APT reconstructed data showing the presence of Li on the surface and at the grain boundaries in the sub-surface region. (b-e) Atom maps from the grey dashed region in (a), revealing the distribution of (b) Li, (c) Li_2O/Li_2F, (d) $CH_x/SO_x/CO_x/N$, and (e) O-containing molecular ions. (f,g) 1D concentration profile plotted along the arrow (f/g) in (a), showing (f) only lithium and copper and (g) O, F, S, C, and N, revealing lithium trapping across the grain interior and grain boundaries. (h,i) 1D concentration profile along the arrow (h/i) in (a), showing (h) only lithium and copper and (i) O, F, S, C and N in the surface regions.

(Figure 5b–d,i). The lithium concentration in the surface is 70.8 ± 0.6 at.% (Figure 5h and Table 1), also higher than that in the 3-cycle copper foil surface (Table 1). More importantly, lithium concentration in the grain interior increases considerably from 0.08 ± 0.01 at.% after three cycles to 0.34 ± 0.01 at.% after eight cycles (Table 1). To further investigate the overall concentration in the copper foil, we summarized the concentrations of lithium and other elements across all APT datasets, including all regions, in Table S2 (four datasets for one cycle; three datasets for three and eight cycles). The overall lithium content increases from 0.27 ± 0.01 to 2.1 ± 0.1 at.% from one to eight cycles. These results indicate that more lithium is trapped in the copper foil as the cycle number increases.

Additionally, oxygen and carbon penetrate deeper into the copper grain interior after eight cycles (~170 nm, as revealed by O/Cu_xO_y mapping in Figure 5e) than after three cycles (~40 nm, Figure 4e). Also, the oxygen and carbon concentration in the grain interior increases to 1.3 ± 0.1 and 0.04 ± 0.01 at.%, respectively, after eight cycles (Table 1, Figure 5g). Note that the oxygen and carbon solubilities in copper are extremely low and have rarely been reported for room temperature [37]. Thus, the creation of defects, vacancies, and dislocations in the copper lattice during plating and stripping is essential for providing trapping sites for oxygen and carbon, which attract lithium during subsequent plating. Previous studies [16–19] had only speculated that lithium might diffuse into grain boundaries, since lithium diffusion through

the copper lattice is sluggish at room temperature. However, no experimental evidence was provided to confirm that the trapping sites are grain boundaries. In our study, we provide direct experimental evidence that lithium is trapped at grain boundaries and boundary junctions as early as after one cycle. More importantly, our study unprecedentedly shows that the top ~100 nm copper foil surfaces become nanocrystalline and defect-rich after a few (three) plating and stripping cycles. These defect sites facilitate the trapping of oxygen and carbon, which together pin the lithium in the copper lattices and grain boundaries during plating and stripping. Detailed characterization of the copper foil after separate plating and plating/stripping is underway to elucidate the diffusion of individual elements into the foil during the iterative processes. Collectively, our TKD, STEM and APT results indicate that cycling induces a defect-rich subsurface copper region that traps lithium along with unexpectedly high levels of oxygen, pointing to a coupled electro-chemo-mechanical degradation mechanism. Such lithium, oxygen, and carbon trapping likely degrades the copper current collector surface, most likely leading to the commonly observed deterioration in battery cell performance, while these findings still need to be re-investigated for other, in particular solid electrolyte systems, as currently underway in our labs.

3 | Conclusion

In summary, our study unveils that lithium is trapped at the boundaries and boundary junctions of the copper current collector after one plating/stripping cycle using an ionic liquid-based electrolyte. The APT data confirm that lithium diffuses into the grain interior, grain boundaries, and boundary junctions, where it can be strongly pinned by forming 3–4 nm-sized lithium-rich clusters. As the cycle number increases, the copper current collector surface undergoes microstructural changes, with the grain size decreasing from a few micrometers after one cycle to tens of nanometers after eight cycles. Such microstructural changes are accompanied by the formation of more defects, e.g., vacancies, dislocations, and interfaces, in the subsurface region of the copper foil, fostering further lithium trapping. Additionally, more oxygen and carbon, along with lithium, are observed in the subsurface region as the cycle number increases. The presence of lithium, oxygen, and carbon in the subsurface regions likely degrades the copper current collector, deteriorating the overall performance as cycling proceeds. We may anticipate that these atomic-scale insights into lithium loss will guide the development of innovative strategies to address the commonly observed (very) low Coulombic efficiencies in zero-excess LMBs, thereby advancing the technology toward eventual commercialization.

4 | Experimental Section

4.1 | Electrolyte Preparation

The electrolyte was composed of a mixture of 1-butyl-1-methyl pyrrolidinium bis(fluorosulfonyl)imide ($PYR_{14}FSI$) and lithium bis(trifluoromethanesulfonyl)imide salt (LiTFSI, 3 M, battery grade) with a ratio of 8:2 ($PYR_{14}FSI$:LiTFSI). $PYR_{14}FSI$ was synthesized according to the procedure reported by Montanino et al. [38]. and dried under vacuum (10^{-3} mbar) for 12 h at 70°C. The lithium salt was dried under vacuum for 12 h at 120°C. Subsequently, the ionic liquid and the salt were mixed in the given ratio to obtain the electrolyte, which was further dried under vacuum for 2 h at room temperature, for 6 h at 50°C, and for 12 h at 80°C. The same procedure was repeated using a turbomolecular pump (10^{-7} mbar) to reduce the water content to a few ppm. Afterward, 5 wt.% fluoroethylene carbonate (FEC; Powerlyte) was added to the electrolyte according to a previous study in our lab, revealing a superior lithium stripping and plating behavior [22].

4.2 | Cell Assembly

Pouch cells for the electrochemical tests were assembled in a dry room environment with a dew point of the incoming air of −70°C. Lithium metal strips (thickness: 500 µm, Honjo Metal Co.) and copper foil (thickness: 40 µm, Welcos) were used as electrodes for the Li||Cu cells. Celgard SV718 (thickness: 25 µm) and glass microfiber sheets (thickness: 260 µm, Whatman, GF/A) were used as separators, with Celgard facing the copper electrode and the glass microfiber sheet facing the lithium-metal electrode. The separators were soaked with 100 µL of the electrolyte. To completely wet the separators and remove any residual air, the cells were placed under vacuum (10^{-3} mbar) for ca. 100 s. The cells were eventually sealed under vacuum. The active area for lithium plating and stripping was 0.785 cm^2. The cell setup is shown in Figure 1a.

4.3 | Electrochemical Characterization

Galvanostatic plating and stripping was conducted using a Maccor battery tester at 40°C. A total areal capacity of 1 mAh cm^{-2} was plated on the Cu electrode at a current density of 0.05 mA cm^{-2} within 20 h after a rest step of 12 h. The plating step was followed by stripping the lithium back to the lithium-metal electrode at the same current density for a maximum of 20 h or until the cut-off voltage of 0.3 V was reached. Either one, three or eight full plating/stripping cycles were conducted.

4.4 | STEM and APT Characterization

For preparing the STEM and APT samples, the cycled pouch cells were opened in a Sylatech GB1500-E glovebox (O_2 and H_2O < 0.1 ppm), and the non-cycled and cycled electrodes were washed five times with 1,2-dimethoxyethane (DME; Sigma Aldrich) to remove any residual electrolyte. The top-down view SEM images were recorded using a FEI Helios G5 CX FIB/SEM at 2 and 10 kV. To prevent samples from oxidation and contamination during sample transfer, the Cu foils were transferred via a customized Ferrovac vacuum transfer suitcase. Afterward, the Cu foil surfaces were covered by a 120 nm thick Cr protective layer via physical vapor deposition coating using a Leica EM ACE600 sputter coater in order to prevent the sample surfaces from ion beam damage during specimen preparation by means of FIB/SEM. The STEM and APT specimens were prepared via standard lift-out procedures by using a FEI Helios G5 CX FIB/SEM. A 300 nm thick carbon film was deposited on the STEM samples by electron beam deposition prior to the lift-out process, followed by a 3 µm thick ion beam assisted carbon deposition. STEM images were recorded

directly via FIB/SEM using a STEM detector at 30 kV. TKD was carried out with a JEOL JSM-7200F SEM at 30 kV with a sample tilt of 10 degree with a step size of 20 nm. The orientation contrast maps were acquired using an Oxford Instruments Symmetry camera controlled via AZtec software. The APT experiments were performed using a Cameca LEAP 5000 XR at a temperature of 65 K in laser mode. The APT specimens were transferred from FIB to APT using a Ferrovac Ultra High Vacuum Cryo Transfer Suitcase (UHVCTS, reaching a pressure of $<1\times10^{-9}$ mbar) to further minimize the oxidation of the APT needles. A laser pulse energy of 40 pJ, a pulse frequency of 125 kHz and a 0.4% detection rate were used as the experimental conditions during the APT acquisition. The reconstruction and APT data analysis were carried out using the AP Suite 6.3.3.55 software.

4.5 | Depth-Resolved X-Ray Photoelectron Spectroscopy (XPS) Analysis

The elemental composition and the chemical state of the elements at the (sub-)surface of the cycled Cu samples (after one plating/stripping cycle and after three cycles) was determined by x-ray photoelectron spectroscopy (XPS) measurements using a Specs XPS system with a Phoibos 150 energy analyser. To avoid any surface contamination, the samples were transferred in inert gas atmosphere to the sample load lock of the XPS system. The measurements were done with monochromatized Al K_a radiation (300 W, 13 kV) and a pass energy of 30 eV at the analyser for the detail spectra. In order to get a depth profile of the elemental concentration, the topmost material was removed by successive Ar^+ ion sputtering. Measurements were collected before sputtering and after 10, 30, and 60 min of sputtering, with the latter being applied only for the sample subjected to three plating/stripping cycles. Charging effects at the surface were negligible and neutralization not necessary. The main C1s peak was set to 284.8 eV to compensate small peak shifts. The peak fit of the XPS results was done with CasaXPS, using Shirley-type backgrounds and Gaussian–Lorentzian (GL30) peak shapes. For the spectra in the Li 1s region, the peaks assigned to Li_2O and LiF were added at 53.8 and 55.6 eV, respectively. Their intensity was calculated based on the intensity of the corresponding peaks in the F 1s and O 1s regions, taking into account stoichiometry and relative sensitivity factors

4.6 | Density Functional Theory (DFT) Calculation

DFT [39, 40] calculations were performed using the Vienna Ab initio Simulation Package (VASP) within the framework of the projector augmented-wave (PAW) method [41, 42]. The exchange–correlation interaction was described using the generalized gradient approximation (GGA) in the form of the Perdew–Burke–Ernzerhof (PBE) functional [43]. A plane-wave basis set with an energy cutoff of 520 eV was employed for bulk and defect calculations to ensure accurate total energies, while a cutoff of 450 eV was used for surface calculations. Electronic self-consistency was achieved with an energy convergence criterion of 2×10^{-4} eV for bulk/defect calculations and 1×10^{-5} eV for surface models. Ionic relaxations were performed using a conjugate gradient algorithm until the forces on each atom were below 0.02 eV $Å^{-1}$. Brillouin zone sampling was performed at the Γ-point [44]. Bulk copper was modeled using a face-centered cubic (fcc) structure. Supercells containing 32 atoms were constructed to investigate lithium incorporation in interstitial, substitutional, and vacancy-containing configurations. For substitutional calculations, a copper vacancy was first introduced, followed by lithium insertion at the vacant site. All structures were relaxed with fixed cell shape and volume.

Spin-polarized calculations were performed throughout with initial magnetic moments assigned to all atoms to ensure numerical stability, although the final magnetic moments were negligible, consistent with the non-magnetic nature of copper. Partial occupancies were treated using the Methfessel–Paxton scheme (ISMEAR = 1) with a smearing width of 0.1 eV for bulk/defect systems and 0.2 eV for surface calculations.

For surface calculations, slab models of copper were constructed with a vacuum region of 20 Å to avoid spurious interactions between periodic images. Structural relaxations were performed while keeping the lattice parameters fixed. Long-range dispersion interactions were included using the DFT-D3 method with Becke–Johnson damping (https://doi.org/10.1002/jcc.21759). Dipole corrections were applied along the surface normal (LDIPOL =.TRUE., IDIPOL = 3) to account for asymmetries in the slab geometry.

The spherical contributions to the gradient corrections inside the PAW spheres were included (LASPH = TRUE.), and the precision of the calculations was set to "Accurate" to ensure reliable total energies. All reported energies correspond to fully relaxed structures.

Author Contributions

T.L. and D.B. conceptualized and supervised the project. C.F. performed APT and STEM measurements. C.F. and T.L. analyzed the APT data. O.A., Z.L., and M.S. prepared the electrolyte and cells, performed the electrochemical measurements, conducted the sample preparation. M.S. carried out the DFT simulation. T.M. carried out the XPS measurements and analysis. A.K. performed the TKD measurements. All authors agreed on the contents and conclusion of the paper.

Acknowledgements

This work is supported by European Research Council (ERC) grants ("INTERACT", Grant Number. 101125947 and "RACER", Grant Number. 10143029). Funded by the European Union. Views and opinions expressed are however those of the author(s) only and do not necessarily reflect those of the European Union or the European Research Council Executive Agency. Neither the European Union nor the granting authority can be held responsible for them. Moreover, this work has been financially supported by the German Federal Ministry of Education and Research (BMBF), now the German Federal Ministry of Research, Technology and Space (BMFTR) within the LILLINT-2 project (03XP0511E) and the HighSafe-III project (03XP0568A). T.L. and C.F. acknowledge Zentrum für Grenzflächendominierte Höchstleistungswerkstoffe (ZGH) at Ruhr University Bochum for the access of infrastructure (Cameca LEAP 5000 XR, FEI Helios G5 CX SEM/FIB and JEOL JEM-2200FS). T.L. thanks Deutsche Forschungsgemeinschaft (DFG, German Research Foundation) – project number 467717439 for establishing cryogenic ultra-high vacuum sample transfer solution. T.L. thank Dr. Hosseini for assistance with sample delivery. M.S. acknowledges the computational resources

provided by the state of Baden-Württemberg through bwHPC and by the German Research Foundation (DFG) through Grant Number. INST 40/575-1 FUGG (JUSTUS 2 cluster).

Open access funding enabled and organized by Projekt DEAL.

Conflicts of Interest

The authors declare no conflicts of interest.

Data Availability Statement

The source data and raw datasets generated and/or analysed during the current study are available on Zenodo [45].

References

1. B. Liu, J.-G. Zhang, and W. Xu, "Advancing Lithium Metal Batteries," *Joule* 2 (2018): 833–845, https://doi.org/10.1016/j.joule.2018.03.008.

2. A. Varzi, K. Thanner, R. Scipioni, et al., "Current Status and Future Perspectives of Lithium Metal Batteries," *Journal of Power Sources* 480 (2020): 228803, https://doi.org/10.1016/j.jpowsour.2020.228803.

3. T. Wulandari, D. Fawcett, S. B. Majumder, and G. E. Poinern, "Lithium-Based Batteries, History, Current Status, Challenges, and Future Perspectives," *Battery Energy* 2 (2023): 20230030, https://doi.org/10.1002/bte2.20230030.

4. G. Crabtree, E. Kócs, and L. Trahey, "The Energy-Storage Frontier: Lithium-ion Batteries and Beyond," *MRS Bulletin* 40 (2015): 1067–1078, https://doi.org/10.1557/mrs.2015.259.

5. W. Wu, W. Luo, and Y. Huang, "Less Is More: a Perspective on Thinning Lithium Metal towards High-Energy-Density Rechargeable Lithium Batteries," *Chemical Society Reviews* 52 (2023): 2553–2572, https://doi.org/10.1039/D2CS00606E.

6. X. He, D. Bresser, S. Passerini, et al., "The Passivity of Lithium Electrodes in Liquid Electrolytes for Secondary Batteries," *Nature Reviews Materials* 6 (2021): 1036–1052, https://doi.org/10.1038/s41578-021-00345-5.

7. B. Horstmann, J. Shi, R. Amine, et al., "Strategies towards Enabling Lithium Metal in Batteries: Interphases and Electrodes," *Energy & Environmental Science* 14 (2021): 5289–5314, https://doi.org/10.1039/D1EE00767J.

8. S. Li, F. Wu, T. Chen, et al., "Progress and Challenges for Energy-Dense and Cost-Effective Anode-Free Lithium Metal Batteries," *Energy Material Advances* 6 (2025): 0168, https://doi.org/10.34133/energymatadv.0168.

9. S. Nanda, A. Gupta, and A. Manthiram, "Anode-Free Full Cells: a Pathway to High-Energy Density Lithium-Metal Batteries," *Advanced Energy Materials* 11 (2021): 2000804, https://doi.org/10.1002/aenm.202000804.

10. Z. Xie, Z. Wu, X. An, et al., "Anode-free Rechargeable Lithium Metal Batteries: Progress and Prospects," *Energy Storage Materials* 32 (2020): 386–401, https://doi.org/10.1016/j.ensm.2020.07.004.

11. L. Lin, K. Qin, Y.-S. Hu, et al., "A Better Choice to Achieve High Volumetric Energy Density: Anode-Free Lithium-Metal Batteries," *Advanced Materials* 34 (2022): 2110323, https://doi.org/10.1002/adma.202110323.

12. M. Genovese, A. Louli, R. Weber, S. Hames, and J. Dahn, "Measuring the Coulombic Efficiency of Lithium Metal Cycling in Anode-free Lithium Metal Batteries," *Journal of the Electrochemical Society* 165 (2018): A3321–A3325, https://doi.org/10.1149/2.0641814jes.

13. S.-T. Myung, Y. Sasaki, S. Sakurada, Y.-K. Sun, and H. Yashiro, "Electrochemical Behavior of Current Collectors for Lithium Batteries in Non-aqueous Alkyl Carbonate Solution and Surface Analysis by ToF-SIMS," *Electrochimica Acta* 55 (2009): 288–297, https://doi.org/10.1016/j.electacta.2009.08.051.

14. S.-T. Myung, Y. Hitoshi, and Y.-K. Sun, "Electrochemical Behavior and Passivation of Current Collectors in Lithium-ion Batteries," *Journal of Materials Chemistry* 21 (2011): 9891, https://doi.org/10.1039/c0jm04353b.

15. P. Zhu, D. Gastol, J. Marshall, R. Sommerville, V. Goodship, and E. Kendrick, "A Review of Current Collectors for Lithium-ion Batteries," *Journal of Power Sources* 485 (2021): 229321, https://doi.org/10.1016/j.jpowsour.2020.229321.

16. Y. Huang, H. Chen, and L. Nyholm, "Influence of Lithium Diffusion into Copper Current Collectors on Lithium Electrodeposition in Anode-Free Lithium-Metal Batteries," *Small* 19 (2023): 2306829, https://doi.org/10.1002/smll.202306829.

17. D. Rehnlund, F. Lindgren, S. Böhme, et al., "Lithium Trapping in Alloy Forming Electrodes and Current Collectors for Lithium Based Batteries," *Energy & Environmental Science* 10 (2017): 1350–1357, https://doi.org/10.1039/C7EE00244K.

18. S. Lv, T. Verhallen, A. Vasileiadis, et al., "Operando Monitoring the Lithium Spatial Distribution of Lithium Metal Anodes," *Nature Communications* 9 (2018): 2152, https://doi.org/10.1038/s41467-018-04394-3.

19. R. Rupp, B. Caerts, A. Vantomme, J. Fransaer, and A. Vlad, "Lithium Diffusion in Copper," *The Journal of Physical Chemistry Letters* 10 (2019): 5206–5210, https://doi.org/10.1021/acs.jpclett.9b02014.

20. S. Kim, Y. Byun, C. Lee, Y. Lee, E. Lee, and K. Eom, "In-situ Constructing LiF-rich Lithiophilic Interface by Unifying Additive Approach and Electrochemical Treatment for AFLMBs," *Chemical Engineering Journal* 507 (2025): 160406, https://doi.org/10.1016/j.cej.2025.160406.

21. T. Li, A. Devaraj, and N. Kruse, "Atomic-scale Characterization of (electro-)Catalysts and Battery Materials by Atom Probe Tomography," *Cell Reports Physical Science* 3 (2022): 101188, https://doi.org/10.1016/j.xcrp.2022.101188.

22. D. Stępień, B. Wolff, T. Diemant, et al., "Insights into the Lithium Nucleation and Plating/Stripping Behavior in Ionic Liquid-Based Electrolytes," *ACS Applied Materials & Interfaces* 15 (2023): 25462–25472, https://doi.org/10.1021/acsami.3c01722.

23. K. Yan, Z. Lu, H.-W. Lee, et al., "Selective Deposition and Stable Encapsulation of Lithium through Heterogeneous Seeded Growth," *Nature Energy* 1 (2016): 16010, https://doi.org/10.1038/nenergy.2016.10.

24. P. Biswal, S. Stalin, A. Kludze, S. Choudhury, and L. A. Archer, "Nucleation and Early Stage Growth of Li Electrodeposits," *Nano Letters* 19 (2019): 8191–8200, https://doi.org/10.1021/acs.nanolett.9b03548.

25. C. Fang, J. Li, M. Zhang, et al., "Quantifying Inactive Lithium in Lithium Metal Batteries," *Nature* 572 (2019): 511–515, https://doi.org/10.1038/s41586-019-1481-z.

26. Y.-C. Hsieh, M. Leißing, S. Nowak, B.-J. Hwang, M. Winter, and G. Brunklaus, "Quantification of Dead Lithium via in Situ Nuclear Magnetic Resonance Spectroscopy," *Cell Reports Physical Science* 1 (2020): 100139, https://doi.org/10.1016/j.xcrp.2020.100139.

27. G. C. Sneddon, P. W. Trimby, and J. M. Cairney, "Transmission Kikuchi Diffraction in a Scanning Electron Microscope: a Review," *Materials Science and Engineering: R: Reports* 110 (2016): 1–12, https://doi.org/10.1016/j.mser.2016.10.001.

28. K. Wang, N. R. Tao, G. Liu, J. Lu, and K. Lu, "Plastic Strain-induced Grain Refinement at the Nanometer Scale in Copper," *Acta Materialia* 54 (2006): 5281–5291, https://doi.org/10.1016/j.actamat.2006.07.013.

29. K. R. Hebert, "Diffusion of Lithium in Copper Current Collectors of Lithium Metal Anodes in Liquid Cells," *Journal of Power Sources* 617 (2024): 235098, https://doi.org/10.1016/j.jpowsour.2024.235098.

30. J. Seo, J. Lim, H. Chang, et al., "Sustaining Surface Lithiophilicity of Ultrathin Li-Alloy Coating Layers on Current Collector for Zero-Excess Li-Metal Batteries," *Small* 20 (2024): 2402988, https://doi.org/10.1002/smll.202402988.

31. W. Gąsior, B. Onderka, Z. Moser, A. Dębski, and T. Gancarz, "Thermodynamic Evaluation of Cu–Li Phase Diagram from EMF Measurements and DTA Study," *Calphad* 33 (2009): 215–220, https://doi.org/10.1016/j.calphad.2008.10.006.

32. S. Pastorello, "Thermal Analysis of the System Lithium-copper," *Gazzetta Chimica Italiana* 60 (1930): 988–992.

33. S. Zhang, E. Isotta, R. Bueno-Villoro, and C. Scheu, "Probing Grain-boundary Structure, Chemistry, and Transitions," *MRS Bulletin* 51 (2026): 168–180, https://doi.org/10.1557/s43577-025-01041-3.

34. S. Korte-Kerzel, T. J. Rupert, D. S. Gianola, S. Sandlöbes-Haut, and Z. Xie, "Defect Phases beyond Grain Boundaries," *MRS Bulletin* 51 (2026): 202–213, https://doi.org/10.1557/s43577-025-01044-0.

35. Y. Li, F. Börrnert, M. Ghorbani-Asl, et al., "In Situ TEM Investigation of the Lithiation and Delithiation Process between Graphene Sheets in the Presence of Atomic Defects," *Advanced Functional Materials* 34 (2024): 2406034, https://doi.org/10.1002/adfm.202406034.

36. A. H. White and L. H. Germer, "The Rate of Oxidation of Copper at Room Temperature," *Transactions of The Electrochemical Society* 81 (1942): 305, https://doi.org/10.1149/1.3071381.

37. R. Schmid, "A Thermodynamic Analysis of the Cu-O System with an Associated Solution Model," *Metallurgical Transactions B* 14 (1983): 473–481, https://doi.org/10.1007/BF02654367.

38. M. Montanino, F. Alessandrini, S. Passerini, and G. B. Appetecchi, "Water-based Synthesis of Hydrophobic Ionic Liquids for High-energy Electrochemical Devices," *Electrochimica Acta* 96 (2013): 124–133, https://doi.org/10.1016/j.electacta.2013.02.082.

39. P. Hohenberg and W. Kohn, "Inhomogeneous Electron Gas," *Physical Review* 136 (1964): B864–B871, https://doi.org/10.1103/PhysRev.136.B864.

40. W. Kohn and L. J. Sham, "Self-Consistent Equations Including Exchange and Correlation Effects," *Physical Review* 140 (1965): A1133–A1138, https://doi.org/10.1103/PhysRev.140.A1133.

41. G. Kresse and D. Joubert, "From Ultrasoft Pseudopotentials to the Projector Augmented-wave Method," *Physical Review B* 59 (1999): 1758–1775, https://doi.org/10.1103/PhysRevB.59.1758.

42. P. E. Blöchl, "Projector Augmented-wave Method," *Physical Review B* 50 (1994): 17953–17979, https://doi.org/10.1103/PhysRevB.50.17953.

43. J. P. Perdew, K. Burke, and M. Ernzerhof, "Generalized Gradient Approximation Made Simple," *Physical Review Letters* 77 (1996): 3865–3868, https://doi.org/10.1103/PhysRevLett.77.3865.

44. H. J. Monkhorst and J. D. Pack, "Special Points for Brillouin-zone Integrations," *Physical Review B* 13 (1976): 5188–5192, https://doi.org/10.1103/PhysRevB.13.5188.

45. L. Tong and B. Dominic, "Data of Lithium Loss in the Copper Foil," *Zenodo* 23 (2026), https://doi.org/10.5281/zenodo.20810096.

Supporting Information

Additional supporting information can be found online in the Supporting Information section.

Supporting File 1: aenm71291-sup-0001-SuppMat.pdf.

Supporting File 2: aenm71291-sup-0002-VideoS1.mp4.

Supporting File 3: aenm71291-sup-0003-VideoS2.mp4.

Supporting File 4: aenm71291-sup-0004-VideoS3.mp4.

Supporting File 5: aenm71291-sup-0005-VideoS4.mp4.